Current Applied Physics 14 (2014) 439–446

Contents lists available at ScienceDirect

Current Applied Physics

journal homepage: www.elsevier.com/locate/cap

Selective ethanol gas sensing behavior of mesoporous n-type semiconducting $FeNbO_4$ nanopowder obtained by niobium–citrate process

C. Balamurugan [a], A.R. Maheswari [b], D.W. Lee [a,*], A. Subramania [c]

[a] MEMS and Nanotechnology Laboratory, School of Mechanical Engineering, Chonnam National University, Gwangju 500757, Republic of Korea
[b] PG and Research Department of Chemistry, J.J. College of Arts and Science, Pudukkottai 622 422, India
[c] Centre for Nanoscience and Technology, Pondicherry University, Puducherry 605 014, India

ARTICLE INFO

Article history:
Received 27 August 2013
Received in revised form
15 November 2013
Accepted 30 November 2013
Available online 14 December 2013

Keywords:
$FeNbO_4$
Ethanol sensor
Mesoporous nanocrystalline
Niobium–citrate process
n-Type semiconductor

ABSTRACT

Beyond the most investigated mesoporous silica and carbon based materials, metal oxides have attracted considerable interest due to their more diverse electronic functionality, which includes gas sensing activities, semiconductor characteristics and magnetic properties. In this paper, we describe the fabrication, characterization and application of mesoporous $FeNbO_4$ nanopowder for ethanol gas sensing application. $FeNbO_4$ nanopowder was synthesized via the niobium–citrate complex method, without using any surfactant and size selection medium. Thermal stability and structure of the nanopowder was analyzed by thermogravimetric analysis (TG/DTA) and X-ray diffraction analysis (XRD). Structural analysis confirmed the formation of $FeNbO_4$ with monoclinic structure. The particle size, electrical and optical properties were also systemically investigated by means of transmission electron microscopy (TEM), impedance and diffused reflectance spectra. Nitrogen adsorption isotherms of the $FeNbO_4$ were type IV with hysteresis loops of type H_3 indicating well-defined pore structure with mesoporous nature. The sensing characteristics of $FeNbO_4$ nanopowder such as sensitivity, operating temperature and response time, were studied in the presence of ethanol (C_2H_5OH). Experimental result confirmed that a higher response to ethanol at relatively lower operating temperature of 200 °C.

1. Introduction

Semiconductor metal oxide is one of the most interesting materials for gas sensing applications. Recently, some composite oxides such as $CuNb_2O_6$, $FeTaO_4$, $FeWO_4$ and $FeNbO_4$ [1,2] were found to be more effective in terms of better sensitivity and selectivity to reducing gases. In addition, $FeNbO_4$ semiconducting oxides have been studied extensively for a variety of applications. These include photo anode materials with potential applications in the conversion of solar energy and gas sensors [3]. Moreover, they are well known as the key precursor for successful preparation of single phase perovskite $Pb(Fe_{1/2}Nb_{1/2})O_3$, which is important for multilayer ceramic capacitor applications [4]. $FeNbO_4$, as a functional n-type semiconductor, has stimulated great research interest due to its unique optical and electrical properties. It exhibits semiconducting and magnetic behavior owing to coexistence of Fe^{2+} and Fe^{3+} ions. Most importantly, $FeNbO_4$ structure has been established as a promising material for detecting gases [5,6]. However, the methods reported previously for preparing $FeNbO_4$ utilizes conventional solid state reactions [7]. These methods are quite labor intensive and requires high temperature which can lead to large agglomerations of particles and low surface area. Among the various synthesis methods, chemical-based methods provide a convenient and simple approach for the synthesis of nanoscale materials [8]. It is well known that the response of gas sensors can be improved by decreasing the particle size of the gas-sensing material. This is caused by the increase of number of oxygen sites on its surfaces.

For sensing of ethanol (C_2H_5OH), several metal oxides such as tin oxide, cadmium–iron oxides, cadmium–tin oxides, nickel–tin oxides have been used [9]. These sensors have been used in a wide range of areas such as chemical, biomedical, food industries, wine-quality monitoring, and breath analysis [10]. In these applications, it is desired that the ethanol vapor sensors exhibit features such as high sensitivity, selectivity, stability, low working temperature, fast response and recovery times. Therefore, a great deal of research effort has been devoted to the development of functional materials that may be exploited for the construction of high-performance ethanol vapor sensors.

* Corresponding author. Tel.: +82 62 530 1684.
E-mail address: mems@jun.ac.kr (D.W. Lee).

1567-1739/$ – see front matter © 2013 Elsevier B.V. All rights reserved.
http://dx.doi.org/10.1016/j.cap.2013.11.052

Mesoporous materials have been extensively investigated in the last two decades because of their uniform pore sizes, tuneable pore structures, ease of functionalization and large surface areas. Beyond the most-investigated silica and carbon based materials, metal oxides have attracted considerable interest due to their more diverse electronic functionality [11]. In this paper, we report for the first time ethanol gas sensing phenomena observed in mesoporous nanocrystalline $FeNbO_4$, prepared by the niobium–citrate complex process. Products obtained in this way are generally more homogenous, have higher surface area and finer particle size. Most importantly, it exhibits mesoporosity, higher degree of crystallinity and purity along with lower temperature sinterability than that of powders prepared by conventional methods. These properties enhance ethanol sensing of $FeNbO_4$ prepared by niobium–citrate complex process.

In this work sensitivity of the $FeNbO_4$-based sensor was studied by measuring the resistance of sensor material in air and then in reducing gas environment. Results indicate that the sensor is highly sensitive to ethanol molecules. It also exhibits high response and quick response-recovery time at 200 °C.

2. Preparation of $FeNbO_4$ nanopowder

Two step procedures were followed. The first step involves the preparation of hydrated Nb_2O_5 from Nb_2O_5. Nb_2O_5 was dissolved in HF to form $[NbOF_5]^{2-}$ or $[NbF_7]^{2-}$ complexes [12]. To this, a freshly prepared aqueous solution of ammonium oxalate was added in excess and then aqueous NH_3 was added drop by drop to get hydrous niobium oxide ($Nb_2O_5 \cdot nH_2O$) as precipitate. The precipitate was filtered and washed with 10% aqueous NH_3 by using a centrifuge. The second step involves the dissolution of hydrated Nb_2O_5 in citric acid with the mole ratio of [CA/Nb = 2:1] using H_2O_2 as a catalyst. A clear yellow-colored peroxo-citro-niobate was formed. This yellow color solution was mixed with ferric nitrate in the stoichiometric mole ratio of [Fe/Nb] = 1:1 and the pH of the final solution was adjusted to 7 using NH_4OH. The mixture was heated at about 200 °C to get dried black fluffy mass. The resultant black mass was calcined at 800 °C for 2 h (at a heating rate of 5 °C/min) to get nanosized $FeNbO_4$ with monoclinic phase.

3. Characterization of $FeNbO_4$ powder

Thermogravimetric analysis (TGA) and differential thermal analysis (DTA) were carried out with (Model: Pyris Diamond) under air atmosphere at a heating rate of 10 °C/min from 30 to 900 °C. The phase identification of the calcinated powder was performed using X-ray diffractometer (Model: X' pert-pro diffractometer) with nickel filtered Cu Kα radiation as a source and operated at 40 kV. The powder was scanned in 2θ ranging from 10° to 70° with 0.02° step. The crystallite size of the samples was calculated by Debye–Scherrer's equation. The surface morphology of the powder was analyzed using scanning electron microscopy (Model: Hitachi, SN-3400N). Energy dispersive X-ray (EDAX) spectroscopy was used for identifying the elemental composition of the $FeNbO_4$ at 10 KV accelerating voltage. The particle size of the synthesized powder was confirmed by transmission electron microscopy (Model: Philips, CM-20) at 200 kV. For TEM investigation, $FeNbO_4$ powder was dispersed in ethanol and the solution was agitated by ultrasonic waves to disperse the powder. A drop of this suspension was evaporated into holey carbon coated copper grid. Optical characterization was carried out using UV–vis absorption spectra (Model: Varian, Cary-5000) equipped with a diffuse reflectance accessory. For conductivity measurements, the synthesized $FeNbO_4$ nanopowder was mixed with a few drops of polyvinyl alcohol solution and the mixture was pressed into pellet of 10 mm diameter with 1.5–2 mm thickness using a die at 150 MPa. The pellet was then heated at 400 °C for 1 h to remove the residual polymer which helps to produce porous solid. Conductivity was measured using a computer controlled impedance analyzer (Model: micro auto lab type III) over a range of temperature (30–175 °C) in the frequency range of (1 Hz–500 KHz).

4. Fabrication of the sensors

To evaluate gas-sensing properties, the calcined $FeNbO_4$ powder was mixed with 2% polyvinyl alcohol to make a paste. The resulting fresh paste was coated on alumina tube as the substrate equipped with two platinum wire electrodes 8 mm apart and leads for electrical contacts. The tube was about 8 mm in length, 2 mm in external diameter and 1.6 mm in internal diameter. The sensor element was sintered at 500 °C for 1 h, to make it rigid and to impart porous properties. A small nichrome alloy coil was placed inside the tube and heated to generate the required operating temperatures. A chromel–alumel thermocouple (TC) was used to monitor the operating temperature of the sensor. The output of the thermocouple was connected to a digital temperature indicator. The schematic of sensor element used for the gas sensitivity studies is as shown in Fig. 1. The gas sensing performance of the sensor was studied in a sealed test chamber (300 cm^3) made up of aluminum with a gas inlet and outlet. The concentrations of the test gases were obtained by diluting them with fresh air. The test gas was injected into the test chamber through an injection part and the corresponding change of electrical resistance of the material was measured as a function of time till a constant resistance value was achieved. Then the chamber was purged with air and the experiment was repeated. The electrical resistance was measured both in the presence and absence of the test gas by means of conventional circuit in which the load resistor (RL = 1 MΩ) was connected in series at a circuit voltage of 10 V. The electric circuit for the gas response measurement is shown in Fig. 2. The value of the sensor resistance was measured by monitoring the output voltage across the load resistor changed with the concentrations of the test gas. The sensor response (S) was calculated using the following equation [13,14]:

$$S(\%) = \frac{(R_g - R_a)}{R_a} \times 100, \quad (1)$$

where R_g is the resistance under a given gas concentration at constant temperature and R_a is the base resistance at constant temperature under gas free atmosphere (dry air), respectively.

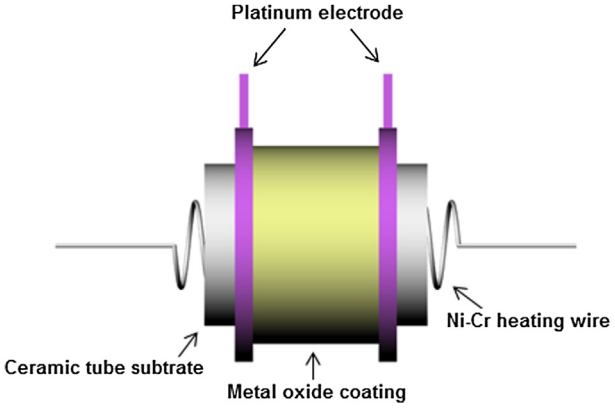

Fig. 1. The schematic of sensor element used for the gas response studies.

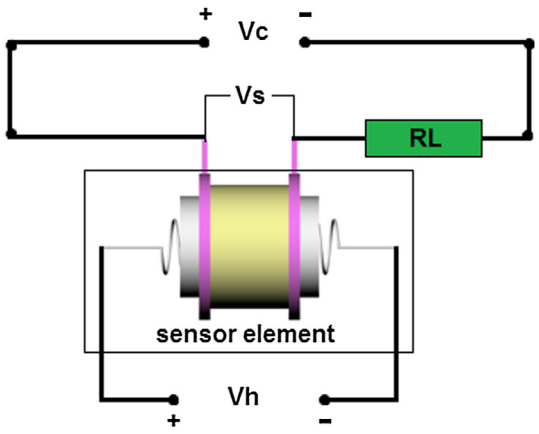

Fig. 2. Electrical circuit of the gas response test system (Vh: heating voltage, Vc: circuit voltage, Vc: output signal voltage and RL: load resistance).

5. Results and discussion

5.1. Thermal analysis

Fig. 3 shows the DTA and TGA curves of the precursor powder synthesized by the niobium citrate complex process. A broad endothermic peak was observed around 145 °C on the DTA curve corresponding to a weight loss of 14% occurring on the TGA curve. This might be ascribed to the removal of water molecules present in the precursor. The sharp exothermic peak at 244 °C could be due to the reaction of nitrates with citric acid. During the reaction, large amounts of gases, such as H_2O, CO_2 and N_2 are liberated resulting in a noticeable weight loss in the TG plot. As the process of heating was continued, two distinguishable endothermic transformations at 276 and 365 °C might be due to the decomposition of remaining organic constituents in the precursor. At 318 and 410 °C, two pronounced exothermic peaks appearing in the DTA probably corresponded to the oxidation of metal cations and to the gradual crystallization process of $FeNbO_4$. TGA curve shows that the sample gradually lost weight below 430 °C. Over the temperature of 430 °C, there was no additional loss of mass. This indicates that decomposition of the precursor was complete at 430 °C.

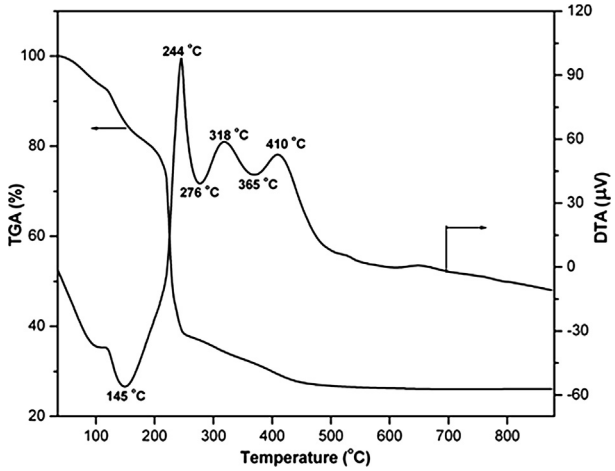

Fig. 3. TG/DTA cures of $FeNbO_4$ precursor.

5.2. X-ray diffraction

The XRD patterns show the crystallization of $FeNbO_4$ powder calcinated at various temperatures from 600 °C to 800 °C for 1 h (Fig. 4). Significant diffraction peaks (111, 120, 122, and 231) for the precursor of $FeNbO_4$ begin to appear when calcined at 600 °C. When the sample calcined at temperature 700 °C, the peaks emerged at 2θ values of 21.76, 23.66 and 27.50 (JCPDS Card No. 73-1610) due to the individual oxide of $Nb_{12}O_{29}$ present along with $FeNbO_4$. This indicates that the reaction is incomplete. The absence of any additional diffraction lines of the powder calcined at 800 °C for 1 h confined a pure monoclinic phase of $FeNbO_4$. This is considerably a lower temperature to obtain the monoclinic phase of $FeNbO_4$ compared with previous report [7,15]. The entire peaks are well consistent with standard JCPDS data (Card No. = 71-1849) [16]. The calculated lattice parameters, such as $a = 4.985$ Å, $b = 5.602$ Å and $c = 4.632$ Å, were in close agreement with the standard lattice parameter values. The average crystallite size of the powders was calculated by Debye–Scherrer's formula;

$$D = k\lambda/\beta \cos\theta, \tag{2}$$

where D is the crystallite size in nm, λ is the radiation wavelength (0.15405 nm for Cu Kα), β is the corrected halfwidth, and θ is the diffraction peak angle, respectively. The average crystallite size of

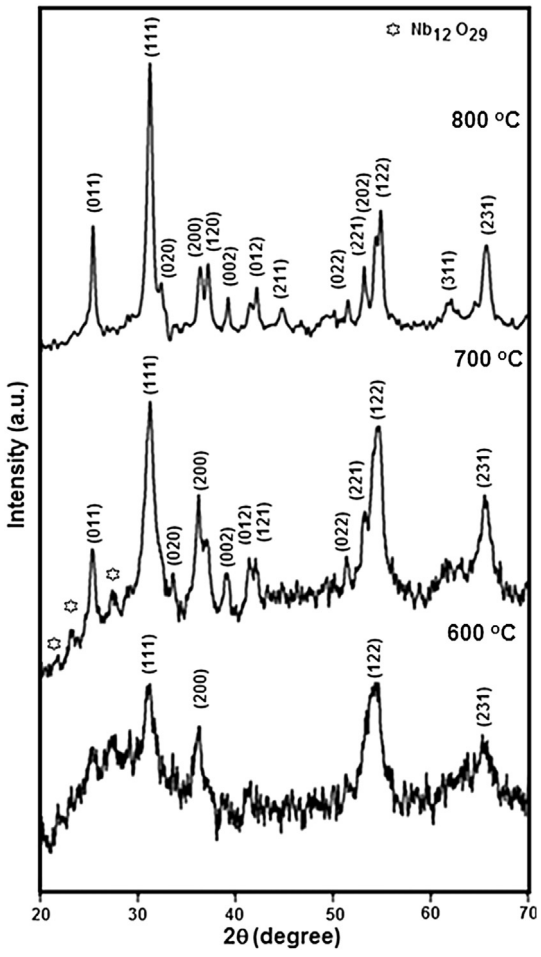

Fig. 4. X-ray diffraction patterns of $FeNbO_4$ precursor calcined at (a) 600 °C, (b) 700 °C, and (c) 800 °C.

$FeNbO_4$ after heat treatment at 800 °C for 1 h was found to be 34 nm.

5.3. SEM studies

Fig. 5(a) shows the surface morphology of $FeNbO_4$ nanopowder calcined at 800 °C for 1 h. The low-magnification SEM image clearly shows that the porous morphology of the product. The high-magnification SEM image shown in Fig. 5(b) confirms the aggregates of nanocrystallites. These aggregates appeared to be formed from particles of size smaller than 34 nm as indicated by XRD data. These nanoparticles seemed to be randomly oriented in irregular fashion to minimize the steric electric charge repulsions thereby resulting in a porous structure. This leads to adsorption of gas molecules in the pores, which in turn causes sensitivity of these sensing elements.

5.4. TEM studies

The calcined powder showed particles with sizes ranging from 30 to 40 nm with the occasional exception of some particles of size >40 nm. Additionally, very small $FeNbO_4$ nanoparticles with a uniform diameter size of 15 nm were observed dispersed along the carbon membrane (of the copper grid). Most of the particles had a spherical shape, and were small particles agglomerate together to form big particles as shown in Fig. 6. The high crystalline quality and size of the particle obtained from TEM are in good agreement with the results obtained from XRD analysis. SAED analysis revealed the polycrystalline nature of these $FeNbO_4$ nanoparticles.

5.5. Energy dispersive X-ray spectroscopy

The chemical composition of the calcined powder was analyzed by energy dispersive X-ray spectroscopy (EDX) equipped with SEM. Fig. 7 shows the EDX result of the sample. The composition ratio of iron, niobium and oxygen are 1.04, 1.01 and 3.95 respectively, which was very close to 1:1:4 for the pure $FeNbO_4$ phase. The composition of the sample obtained from EDX is in good agreement with those observed in the XRD analysis with phase corresponding to $FeNbO_4$. The oxygen deficiencies of the sample could be verified at less than a stoichiometric content of 66.66%. This deficiency made the material useful in sensor applications. In the pure and stoichiometric monoclinic phase of $FeNbO_4$ the Fe and Nb ions are in +3 and +5 valence state, respectively. However, some physical behaviors observed in $FeNbO_4$ are due to oxygen deficiency which leads to the generation of a fraction of Fe^{2+} ions. In recent works [17] reported the detection of mixed valence (Fe^{2+}/Fe^{3+}) of Fe ions in the Fe–O–Fe framework of the monoclinic phase $FeNbO_4$, this facilitated electrical conductivity of the material.

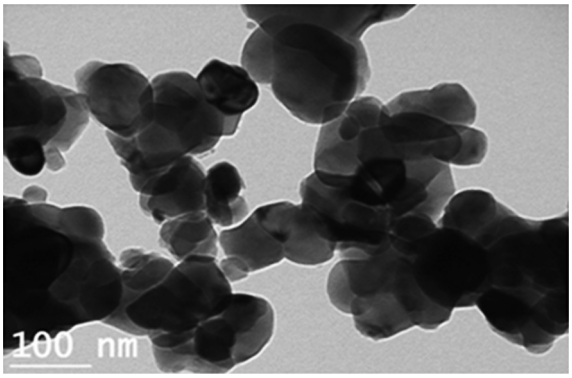

Fig. 6. TEM micrograph of $FeNbO_4$ powder obtained at 800 °C.

5.6. Nitrogen adsorption/desorption measurement

The Brunauer–Emmett–Teller (BET) surface area and pore size distribution of $FeNbO_4$ was obtained from nitrogen adsorption/desorption analysis with a Belsorp II Instrument. Before the measurement, sample was degassed at 220 °C under vacuum for 12 h. The N_2 adsorption/desorption isotherms and the corresponding pore size distribution plots for $FeNbO_4$ nanopowder are shown in Fig. 8. Fig. 8(a) displays a type IV isotherm with type H_3 hysteresis loops in the relative pressure range of 0.70–0.96, suggesting characteristics of mesoporous materials according to IUPAC classification [18]. The pore size distribution was calculated by applying the Barrett–Joyner–Halenda (BJH) method on the desorption branch of isotherm curve Fig. 8(b). From the plot, the pore size shows a broad distribution in the range of 2–160 nm and the pores have a primary size distribution above 2 nm, with a maximum at around 50 nm. Also, a large portion of pores with a narrow size distribution of 2–28 nm has been observed. The specific surface area of the nanopowder was calculated to be 36 m^2/g^{-1} by the Brunauer–Emmett–Teller (BET) method.

5.7. Diffuse reflectance spectroscopy studies

Fig. 9 shows the optical absorption properties of the $FeNbO_4$ nanopowder. The energy band gap of this material was estimated using the adsorption versus wavelength plot. Extrapolation of the linear segment zero absorption gives the absorption edge (λ) value

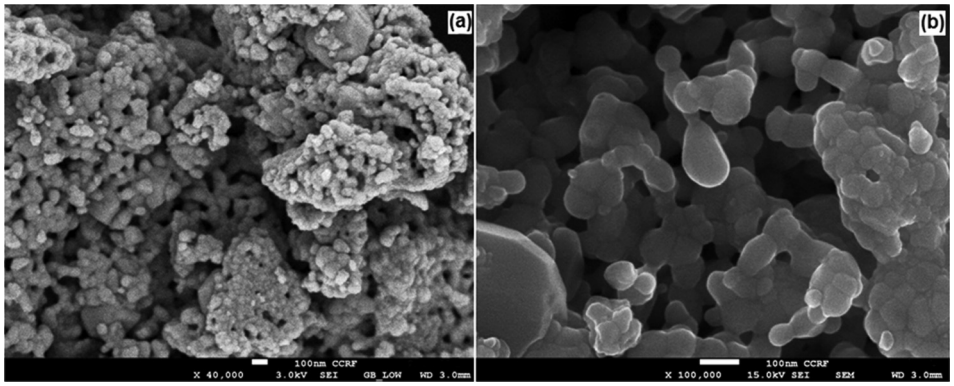

Fig. 5. (a) SEM micrograph of $FeNbO_4$ nanopowder powder obtained at 800 °C and (b) the high-magnification SEM image of nanocrystallites.

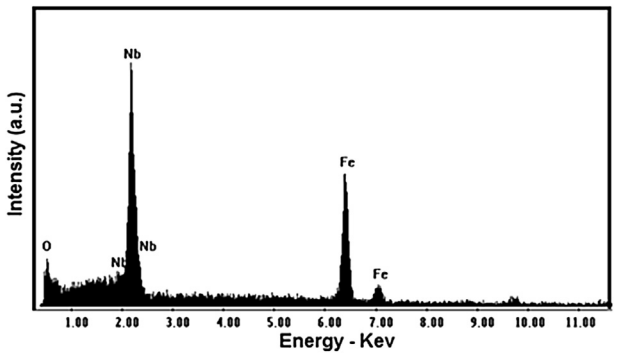

Fig. 7. EDX analysis of $FeNbO_4$ nanopowder obtained at 800 °C.

and it was 640 nm. The optical band gap E_g was calculated using the following relation [19]:

$$E_g = \frac{hc}{\lambda}, \tag{3}$$

where h is Plank's constant (6.626×10^{-34} J s^{-1}), and c is the velocity of light (3×10^8 m/s), respectively. From the above relation, the optical band gap was found to be 1.94 eV.

5.8. Impedance studies

The Nyquist plot obtained for the $FeNbO_4$ powder is shown in Fig. 10. A semicircle was seen in the lower frequency region, this is due to the surface conduction process. The resistivity (R) of the powder was calculated using high frequency data. The intercept at the higher frequency on the x-axis gave the resistivity. The conductivity σ (S cm^{-1}) was calculated using the following relation:

$$\sigma = \frac{l}{RA}, \tag{4}$$

where l is the thickness, A is the surface area of the sample and R is the electrical resistance of the nanopowder, respectively.

Fig. 11 shows an Arrhenius plot of the temperature dependence of the electrical conductivity of $FeNbO_4$ in the temperature range of 30–175 °C in dry air. The linear dependence of σ with temperature is similar to that of a semiconductor. In $FeNbO_4$ nanopowder, the observed semiconducting behavior is due to the oxygen deficiency leading to the generation of Fe^{2+}. The activation energy of the sample was estimated from the slope of the Arrhenius plot and was found to be 0.66 eV.

6. Gas sensing behaviors

The response of typical sensor as a function of operating temperatures is shown in Fig. 12. When the sensor was exposed to reducing gases (600 ppm), the response remarkably increase in the temperature range of 50–200 °C and then gradually decreased in the temperature range of 200–350 °C. The sensor shows no response to gases at the working temperature below 50 °C. This low response at temperatures below 50 °C could be due to insufficient oxygen molecules adsorbed on the sensor surface. When the temperature reached 50 °C, the charge carriers attained sufficient energy to cross the energy barrier and sudden decrease in the resistance was observed. The sensor exhibited highest response to ethanol (600 ppm) at 200 °C (94%) due to enhanced oxidation of ethanol at 200 °C on the surface of the $FeNbO_4$ following the trend of a redox reaction. Beyond this operating temperature, the response decreased due to progressive desorption of previously adsorbed oxygen ionic species. This might also be one of the possible reasons for the decrease in response at above 200 °C temperatures. Additionally, charge carrier concentration and the Debye length of semiconductor material are also influenced by temperature. The sensor response is remarkably high when exposed to the 600 ppm ethanol, while the sensor response is small when exposed to a comparable concentration of interfering gases such as LPG and NH_3; this clearly indicates a selective response of the sensor towards ethanol. This result shows that the $FeNbO_4$ based sensor is highly responsive to ethanol at a low temperature of 200 °C. Therefore, the operating temperature of 200 °C was chosen for further examining the gas-sensing characteristics of the synthesized $FeNbO_4$ nanopowder.

Fig. 13 shows the sensor response to varying gas concentrations levels at fixed operating temperature of 200 °C. The response increases gradually with increasing ethanol concentration and the curve displays a tendency of linearity. Highest response change is observed in 100–200 ppm range as the slope was found to be maximum in this range as shown in Fig. 13. The sensor response is proportional to the number of active centers (adsorption sites) on the surface of sensor. Hence, it can be observed from Fig. 13, the $FeNbO_4$ based sensor element exhibited significant increase in response even at lower concentrations (200 ppm) of ethanol, but once the concentration surpasses 600 ppm, the response increases slowly. This result indicates that the concentration of the adsorbed ethanol molecule is saturated on the limited adsorption sites of the surface. Additionally, the response of sensor depends on removal of adsorbed oxygen molecules by reaction with the ethanol gas and generation of electrons. For a low concentration (<100 ppm) of ethanol exposed on a fixed surface area of the sample, there was a

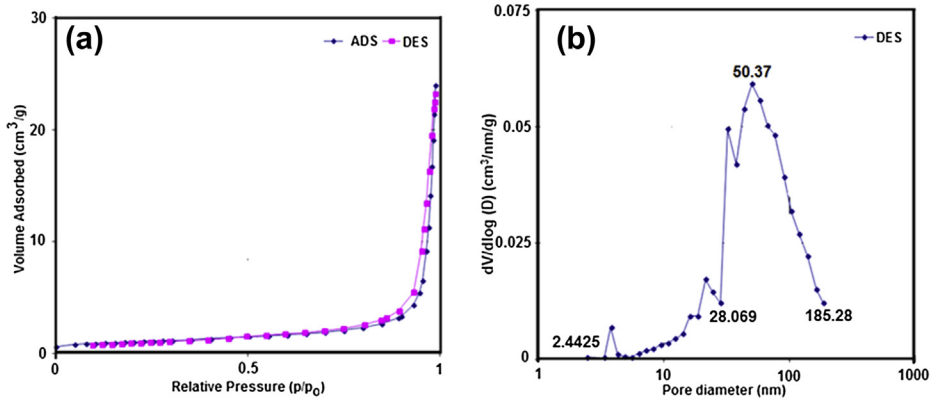

Fig. 8. (a) N_2 adsorption/desorption isotherm of $FeNbO_4$. (b) BJH pore size distribution plots of $FeNbO_4$.

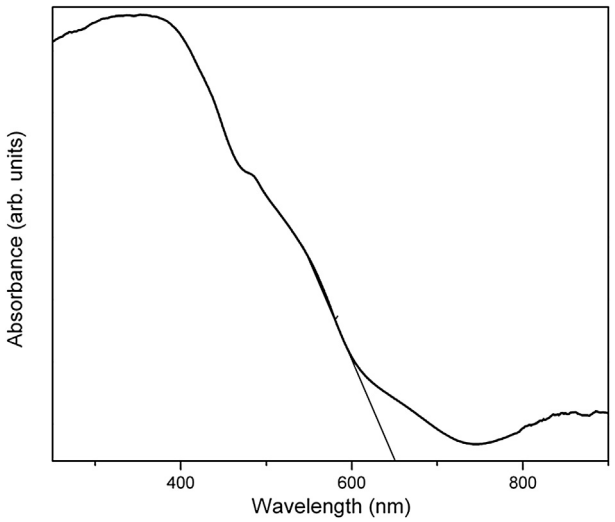

Fig. 9. Complex impedance plot of $FeNbO_4$ nanopowder obtained at 800 °C.

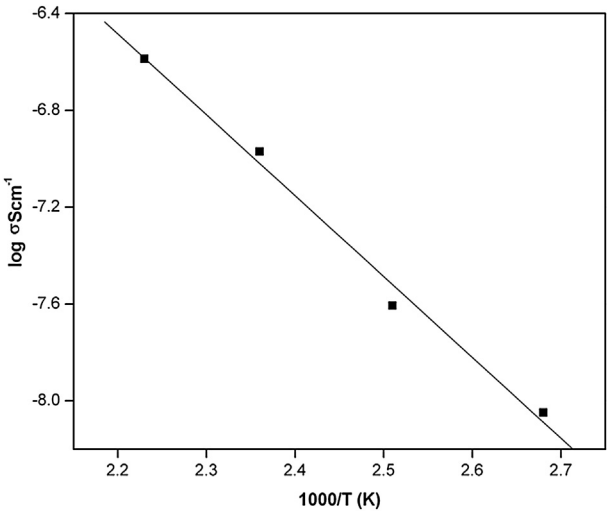

Fig. 11. Diffuse reflection spectra of $FeNbO_4$ nanopowder.

smaller surface coverage by ethanol molecules on the sensor surface and hence lower surface reaction occurred. An increase in ethanol concentration (>100 ppm) enhanced the surface reaction due to larger surface coverage by ethanol molecules, resulting in a rapid change in resistance. On a further increase in concentration (>600 ppm), the surface reaction was saturated due to complete coverage by the ethanol molecules on the surface which leads to a gradual change in resistance.

The response and recovery time were used as characteristic tools. The response time is the time taken to reach the maximum response when the 600 ppm of gas is introduced into the test chamber while keeping the sensor at the optimum operating temperature. The recovery time is the time taken to return back to the initial resistance, when the gas is turned off. Adsorption rate depends on the speed of chemical reaction on the surface of the grains and the speed of diffusion of the gas molecules to that surface and consequently on the pressure. For ethanol, the reaction mechanism is quite complex and proceeds through several intermediate steps $C_2H_5O^-$, $(C_2H_5)_2O$, $C_2H_4O^{2-}$ CH_3CHO as reported previously [20]. It is well known that ethanol consists of the reducing hydrogen species which are bound to carbon. Therefore, ethanol dissociates less easily into reactive reducing component such as hydrogen on the $FeNbO_4$ surface. At an optimum operating temperature the response and recovery characteristic of $FeNbO_4$ sensor was studied by plotting their response as a function of time was shown in Fig. 14. When ethanol vapor was introduced, the response time to reach the maximum response was within 20 s. After the ethanol vapor was removed the response gradually decreased but the recovery time to restore was within 97 s. However, the response and recovery times of the LPG and NH_3, were 17, 38, and 120, 85 s, respectively.

The $FeNbO_4$ based sensor belongs to the surface-controlled type i.e. using the change of surface electrical conductivity to detect gases. Oxygen adsorption plays an important role in the electrical properties of the $FeNbO_4$ sensor. When $FeNbO_4$ is exposed to air, the oxygen molecules interact with the surface in various ways namely physisorption and chemisorption via surface defects and bulk defects. The oxygen vacancy in the $FeNbO_4$ sensor acts as an electron donor to provide electrons to the conduction band of $FeNbO_4$. Physisorption is the weakest form of adsorption to sensor surface, no electrons are exchanged between the sensor material and the oxygen molecules. Hence, the conductivity of the sensor remains unchanged. Usually, physisorption monotonically decreases with increasing operating temperature. At elevated temperature, oxygen molecules are adsorbed on the surface of the

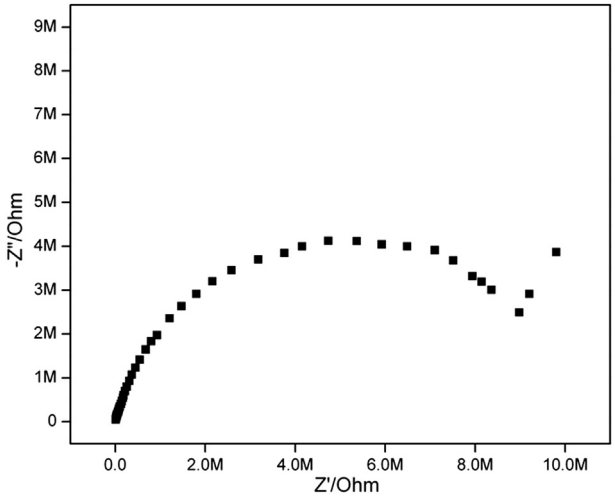

Fig. 10. Arrhenius plot of log conductivity against reciprocal temperature for $FeNbO_4$.

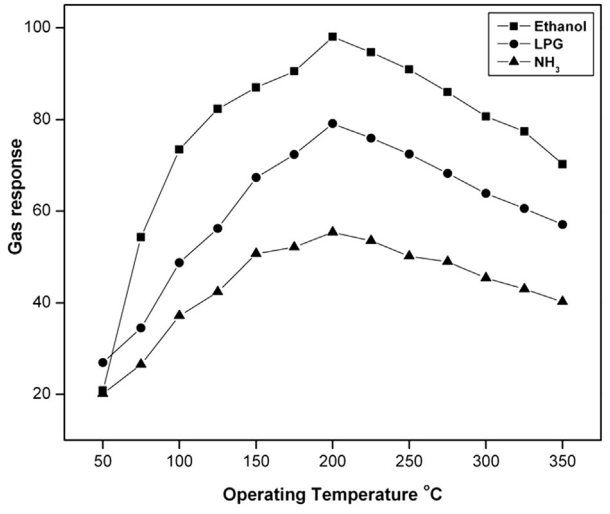

Fig. 12. Gas sensing characteristics of $FeNbO_4$ sensor for ethanol, NH_3 and LPG as a function of various operating temperatures.

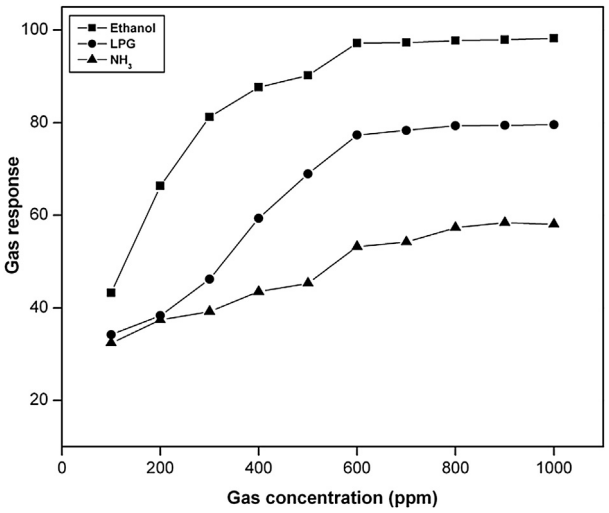

Fig. 13. Sensor response with different concentrations of ethanol, NH_3 and LPG at their optimum operating temperatures.

material and capture free electrons from the conduction band to form chemisorbed oxygen species. The amounts of such chemisorbed oxygen species depend strongly on temperature. The chemisorbed oxygen molecule is dissociated to form O^{2-} and O^- active species at higher temperatures and the O_2 is then disappeared rapidly (Fig. 15(a)). Due to this active superoxo and peroxo species formation, a surface depletion region is created within the oxide matrix. This leads to an increase of the electrical resistance of the sensor material as a result of the diminishment of charge carrier concentration. Due to this electrons transfer mechanism the sensor material undergoes oxidation and loses electrons, whereas pre-adsorbed oxygen molecule receives electrons undergoes reduction. When $FeNbO_4$ is exposed to ethanol, gas molecules can react with adsorbed oxygen species on the surface and effective electron transfer occurs from the ethanol molecules to $FeNbO_4$ i.e. ethanol undergoes oxidation reactions (Fig. 15(b)). As a result, the thickness of the surface depletion region decreases accordingly due to increase of charge carrier concentration, i.e., decreasing electrical resistance of the n-type $FeNbO_4$ semiconductor. The competing reaction of removal electrons by oxygen and the restoration of these electrons by ethanol molecules to $FeNbO_4$ sensing materials can be described as:

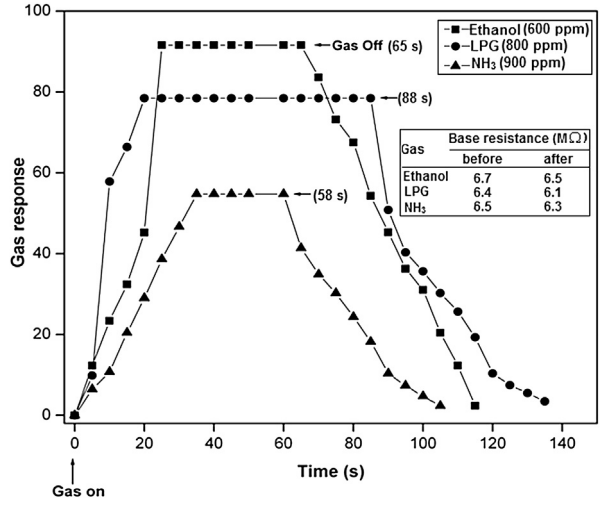

Fig. 14. Ethanol, NH_3 and LPG gas response of $FeNbO_4$ sensor at their optimum operating temperatures.

$$3O_2 + 2e^- \rightarrow 6O^-, \quad (5)$$

$$C_2H_5OH + 6O^- \rightarrow 2CO_2 + 3H_2O + 6e^-. \quad (6)$$

The change in steady-state resistance depends on the adsorption and desorption of oxygen on the surface of sensing materials. An increase in ethanol concentration increases the electron density in the sensing material and decreases the density of adsorbed oxygen molecules (O^-), resulting the decrease in the sensing material resistance value. Electrons released from the above reaction would be captured on either Fe^{3+} or Nb^{5+} or on both, which results in the formation of Fe^{2+} (d^6) or Nb^{4+} (d^1) site in the lattice of $FeNbO_4$. Therefore, the electron transport might occur via Fe^{2+}–O–Fe^{3+} framework with all Nb ions in +5 state, Nb^{4+}–O–Nb^{5+} framework with all Fe ions in +3 state or the combination of both. The higher sensing activity of $FeNbO_4$ nanopowder may be attributed to the fact that besides the one component sites Fe^{3+}–Fe^{2+} and Nb^{5+}–Nb^{4+}, there will be also the mixed sites Fe^{2+}–Nb^{5+} and/or Fe^{3+}–Nb^{4+} ion pairs as a result of mutual charge interaction. From the above discussion the sensing mechanism of $FeNbO_4$ sensor can be summarized as follows:

$$C_2H_5OH + 6O^- \rightarrow CO_2 + H_2O + 6e^-, \quad (7)$$

$$6Fe^{3+} + 6e^- \rightarrow 6Fe^{2+} \quad (8)$$

$$6Nb^{5+} + 6e^- \rightarrow 6Nb^{4+} \quad (9)$$

$$6Fe^{2+} + 6Nb^{5+} \rightarrow 6Nb^{4+} + 6Fe^{3+} \quad (10)$$

As shown in the above mechanism, the presence of fraction amount of reduced Fe^{2+} ions in the system is capable to reduce Nb^{5+} (major center) partly to ions of lower oxidation state, whereas Nb^{4+} minor centers being more active species in ethanol sensing reaction. The presence of niobium seems to stabilize the catalyst structure against oxidation as well as reduction and to permit a very strongly oxidized/reduced sensing material. This leads to easy recovery of the original state of the sensing material. Apart from the semiconducting properties of the sensing materials, the high sensitivity and selectivity characteristic is also related to the acid–base properties of the sensing surface. The presences of Fe atom enhance the basic sites in $FeNbO_4$ surface and promote the sensitivity of the material to ethanol vapor in a very selective way. However, the rate of the surface reaction is in proportion to the number of available adsorption sites on the outer surface of the sensing material. Hence, high surface area, high surface atomic activity, smaller grain size, lower activation energy and mesoporous structure of the $FeNbO_4$ can greatly enhance the number of

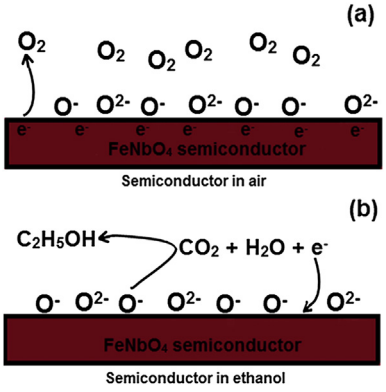

Fig. 15. Schematic diagram of $FeNbO_4$ semiconductor material exposed to air (a) and ethanol gas (b).

the adsorption sites. Additionally, niobium oxides possess a vast reservoir of mobile lattice oxygen, which is capable of increasing active selective sites during gas adsorption and enchaining the response towards ethanol.

7. Conclusions

$FeNbO_4$ nanopowder was synthesized by low temperature niobium citrate complex process. The typical monoclinic structure of $FeNbO_4$ was confirmed by XRD. The product obtained by this preparation method had much lower temperature than the same prepared by the conventional solid state reaction method. The SEM results showed that the sample consists spherical particles with uniform grain size distribution. The TEM results showed that the $FeNbO_4$ had an average particle size of 35 nm. EDX analysis confirmed that the composition of $FeNbO_4$ powder was well matched with the nominal composition. Impedance spectroscopy confirmed the semiconductor behavior for $FeNbO_4$. The diffuse reflection spectra showed that the optical band gap of powder was 2.48 eV. The sensitivity results revealed that $FeNbO_4$ had better response for C_2H_5OH at relatively lower operating temperature of 200 °C. The response time of C_2H_5OH was less than 20 s.

Acknowledgment

This work was supported by the WCU (World Class University) program, through a National Research Foundation of Korea (NRF) grant, funded by the Korea government (MEST) (No. R32-20087).

References

[1] S.K. Biswas, P. Pramanik, Sens. Actuators B 133 (2008) 449.
[2] R. Theissmann, H. Ehrenberg, H. Weitzel, H. Fuess, J. Mater. Sci. 37 (2002) 4431.
[3] R. Theissmann, H. Ehrenberg, H. Weitzel, H. Fuess, Solid State Sci. 7 (2005) 791.
[4] O. Raymond, R. Font, N. Suarez, J. Portelles, J.M. Siqueiros, Ferroelectrics 294 (2003) 141.
[5] D.H. Dawson, D.E. Williams, J. Mater. Chem. 6 (1996) 409.
[6] G.S. Henshaw, I. Morris, I.J. Gellman, D.E. Williams, J. Mater. Chem. 6 (1996) 1883.
[7] K.I. Gnanasekar, V. Jayaraman, E. Prabhu, T. Gnanasekaran, G. Periaswami, Sens. Actuators B 55 (1999) 170.
[8] In-Sun Cho, Sangwook Lee, Jun Hong Noh, Geun Kyu Choi, Hyun Suk Jung, Dong Wan Kim, Kug Sun Hong, J. Phys. Chem. C 112 (2008) 18393.
[9] M. Faisal, Sher Bahadar Khan, Mohammed M. Rahman, Aslam Jamal, Abdullah M. Asiri, M.M. Abdullah, Chem. Eng. J. 173 (2011) 178.
[10] Peiguang Hu, Guojun Du, Weijia Zhou, Jingjie Cui, Jianjian Lin, Hong Liu, Duo Liu, Jiyang Wang, Shaowei Chen, ACS Appl. Mater. Interfaces 2 (2010) 3263.
[11] Xiaohong Sun, Yifeng Shi, Peng Zhang, Chunming Zheng, Xinyue Zheng, Fan Zhang, Yichi Zhang, Naijia Guan, Dongyuan Zhao, Galen D. Stucky, J. Am. Chem. Soc. 133 (2011) 14542.
[12] K. Bhattacharyya, A.K. Tyagi, J. Alloy Compd. 470 (2009) 580.
[13] http://goldbook.iupac.org/S05606.html.
[14] S. Roy Morrison, M.J. Madou, Chemical Sensing with Solid State Devices, Academic Press, London, 1989.
[15] Supon Ananta, Rik Brydson, Noel W. Thomas, J. Eur. Ceram. Soc. 19 (1999) 489.
[16] PCPDFWIN Version 2.4, JCPDS-ICDD, 2003.
[17] G. Alvarez, R. Font, J. Portelles, O. Raymond, R. Zamorano, Solid State Sci. 11 (2009) 881.
[18] Yang Jiao, Feifei Wang, Xiaoming Ma, Qinghu Tang, Kui Wang, Yuming Guo, Lin Yang, Micropor. Mesopor. Mater. 176 (2013) 1.
[19] C. Balamurugana, E. Vijayakumar, A. Subramania, Talanta 88 (2012) 115.
[20] Wen Zeng, Bin Miao, Qu Zhou, Liyang Lin, Physica E 47 (2013) 116.